

# Interaction of Nonlinear Ekman Pumping, Near-Inertial Oscillations, and Geostrophic Turbulence in an Idealized Coupled Model

YANXU CHEN,<sup>a</sup> DAVID STRAUB,<sup>a</sup> AND LOUIS-PHILIPPE NADEAU<sup>b</sup>

<sup>a</sup> *Department of Atmospheric and Oceanic Sciences, McGill University, Montreal, Quebec, Canada*

<sup>b</sup> *Institut des sciences de la mer de Rimouski, Université du Québec à Rimouski, Rimouski, Quebec, Canada*

(Manuscript received 29 October 2020, in final form 17 December 2020)

**ABSTRACT:** A new coupled model is developed to investigate interactions among geostrophic, Ekman, and near-inertial (NI) flows. The model couples a time-dependent nonlinear slab Ekman layer with a two-layer shallow water model. Wind stress forces the slab layer and horizontal divergence of slab-layer transport appears as a forcing in the continuity equation of the shallow water model. In one version of the slab model, self-advection of slab-layer momentum is retained and in another it is not. The most obvious impact of this explicit representation of the surface-layer dynamics is in the high-frequency part of the flow. For example, near-inertial oscillations are significantly stronger when self-advection of slab-layer momentum is retained, this being true both for the slab-layer flow itself and for the interior flow that it excites. In addition, retaining the self-advection terms leads to a new instability, which causes growth of slab-layer near-inertial oscillations in regions of anticyclonic forcing and decay in regions of cyclonic forcing. In contrast to inertial instability, it is the sign of the forcing, not that of the underlying vorticity, that determines stability. High-passed surface pressure fields are also examined and show the surface signature of unbalanced flow to differ substantially depending on whether a slab-layer model is used and, if so, whether self-advection of slab-layer momentum is retained.

**KEYWORDS:** Ekman pumping/transport; Instability; Ocean dynamics; Shallow-water equations

## 1. Introduction

At scales near the deformation radius and larger, near-surface ocean flow can be thought of as a superposition of geostrophic, Ekman, and near-inertial (NI) components, and each of these can interact with the other two. Much attention has been given to how geostrophic currents modify both Ekman and near-inertial flows, and a brief review of previous work is given below. By contrast, Ekman–NI interactions have received less attention. Here, we consider an idealized model in which all three of these flow types interact, although our main focus will be on Ekman–NI and Ekman–geostrophic nonlinearities.

Geostrophic modification of Ekman transport and pumping is the subject of nonlinear Ekman theory. Pioneering work by Stern (1965) considered a uniform wind stress  $\tau$  blowing over a geostrophic vortex and found the pumping velocity to go like  $\nabla \cdot [(\tau \times \hat{z})/(f + \zeta)]$ , where  $f$  is the Coriolis parameter and  $\zeta$  is the relative vorticity associated with the vortex. Other work has focused on straight jets and has extended solutions to higher order (Niiler 1969), compared along- and across-stream stresses (Lee et al. 1994), used vorticity dynamics to examine interactions with stratification (e.g., Thomas and Rhines 2002), and examined higher-order Rossby number effects on the pumping velocity (Hart 2000) and the vertical thickness of the Ekman layer (Pedlosky 2008). More recently, Wenegrat and Thomas (2017) revisited solutions for curvilinear flows such as vortices and meandering jets. Somewhat counterintuitively, they pointed out that Stern's result above does not imply that the transport goes like  $(\tau \times \hat{z})/(f + \zeta)$ . Of more direct interest

to us, their solutions produced complex and interesting structures that could not be expressed in terms of spatially local fields such as  $\tau$  and  $\zeta$ . Instead, nonlocal effects influence the solution. [Nonlocality has also been suggested by Hart (2000) and Pedlosky (2008).] Apart from these nonlinear Ekman effects, geostrophic currents can also impact Ekman transport more directly in that the stress itself depends on both current velocities (e.g., Duhaut and Straub 2006; Dawe and Thompson 2006; Zhai et al. 2012) and sea surface temperature (e.g., Small et al. 2008; Chelton and Xie 2010; O'Neill et al. 2012; Grooms and Nadeau 2016). A series of studies has compared and discussed these effects in the context of eddy–wind interactions (McGillicuddy et al. 2007; Mahadevan et al. 2008; McGillicuddy et al. 2008; Gaube et al. 2015).

Also well appreciated in the literature is that geostrophic currents profoundly influence near-inertial oscillations. Inertial oscillations introduced by large horizontal scale winds, for example, quickly develop smaller horizontal scales due to both  $\beta$  effect (D'Asaro 1989) and the relative vorticity of mesoscale structures (e.g., Perkins 1976; Kunze 1985; van Meurs 1998; Elipot et al. 2010). Recent progress has been summarized by Asselin and Young (2020), who made use of a reduced model similar to that used by Xie and Vanneste (2015) and based on the model of Young and Jelloul (1997, hereafter YBJ). Simulations initialized by adding horizontally uniform inertial oscillations to geostrophic turbulence show near-inertial energy to be quickly imprinted on mesoscale eddies by refraction (Rocha et al. 2018; Asselin and Young 2020). Wave propagation then redistributes this energy horizontally, evacuating it from cyclones and concentrating it into anticyclones. In the anticyclones, a further collapse in horizontal scale serves to increase the vertical group velocity of the waves (see Gill 1984), thus allowing wave energy to exit

Corresponding author: Yanxu Chen, yanxu.chen@mail.mcgill.ca

the surface layer in inertial drain pipes similar to those predicted by [Kunze \(1985\)](#).

Another approach to modeling geostrophic–NI interaction has been to make use of slab models (e.g., [D’Asaro 1985](#); [Klein and Hua 1988](#); [Alford 2001, 2003](#); [Whitt and Thomas 2015](#); [Jing et al. 2017](#)). These models lack wave propagation but do allow for refractive and advective effects. Of particular interest to us is an early result in which [Weller \(1982\)](#) analyzed a slab-layer model<sup>1</sup> to show that the order Rossby number divergence of a geostrophic flow can lead to growth or decay of near-inertial oscillations. In the surface layer, the background flow available to interact with near-inertial oscillations is not limited to geostrophic currents, but also includes a strongly divergent Ekman-like component. It thus seems plausible that an instability similar to that described by Weller may also result from Ekman–NI interactions, and one of our key results will be to show that this is in fact the case.

In this work, we consider different versions of a slab model and then couple these to a two-layer shallow water model. The coupling is two-way. The upper-layer velocity of our two-layer model is the equivalent of the background geostrophic flows described above. The slab itself contains both high and low frequencies, the equivalents of near-inertial oscillations and nonlinear Ekman transport in the setting we propose. One version of the slab model allows for self-advection of slab-layer momentum, thus allowing these low- and high-frequency bands of the slab-layer flow to interact. Each of these also interacts with the interior flow, as represented by the two-layer model. To our knowledge, this is the first model that considers a two-way coupling between the slab and interior dynamics.

The paper is organized as follows. The experimental design and model details, including the two versions of our slab model and how they are coupled to the two-layer model, are presented in [section 2](#). A steady wind stress excites baroclinically unstable jets and transient forcing adds near-inertial oscillations to a highly idealized model configuration. [Section 3](#) presents results. We find statistical equilibria under steady forcing to be relatively insensitive to whether a slab or body force is used to drive the two-layer model. The choice of forcing does, however, significantly impact both the spinups to equilibrium under steady forcing and equilibrium solutions when additional transient forcing is added. In particular, robust differences are found in the unbalanced part of the flow. We hypothesize that these differences are related to an instability similar to that described by Weller. How the differences appear in surface pressure fields is also considered, as this might lend insight into the context of the upcoming Surface Water and Ocean Topography (SWOT) mission ([Gaultier et al. 2016](#);

[Torres et al. 2018](#); [Morrow et al. 2019](#)). A brief discussion is offered in [section 4](#).

## 2. Model

### a. The two-layer shallow water model

In this section, we present a two-layer shallow water model to which wind forcing can be applied either as a body force or via the intermediary of a frictional slab layer embedded in the upper layer of the two-layer model. Denoting the upper- and lower-layer horizontal velocities as  $\mathbf{u}_1$  and  $\mathbf{u}_2$ , we have

$$\begin{aligned} \frac{\partial}{\partial t} \mathbf{u}_1 + (\mathbf{u}_1 \cdot \nabla) \mathbf{u}_1 + f \hat{\mathbf{z}} \times \mathbf{u}_1 &= -\nabla \phi_1 + \mathbf{D}_1 + \delta_{\text{BF}} \frac{\boldsymbol{\tau}}{\rho_0 d_1}, \\ \frac{\partial}{\partial t} \mathbf{u}_2 + (\mathbf{u}_2 \cdot \nabla) \mathbf{u}_2 + f \hat{\mathbf{z}} \times \mathbf{u}_2 &= -\nabla \phi_2 + \mathbf{D}_2, \\ \frac{\partial}{\partial t} d_1 + \nabla \cdot (\mathbf{u}_1 d_1) &= (\delta_{\text{BF}} - 1) \nabla \cdot \mathbf{U}_s, \\ \frac{\partial}{\partial t} d_2 + \nabla \cdot (\mathbf{u}_2 d_2) &= 0, \end{aligned} \quad (1)$$

where  $\rho_0$  is the density of seawater and the coefficient  $\delta_{\text{BF}}$  is a switch. When  $\delta_{\text{BF}}$  is set to one, wind forcing is applied as a body force (BF) distributed over the upper layer. When it is zero, wind stress is instead applied to a slab layer and divergence of the resulting slab-layer transport,  $\nabla \cdot \mathbf{U}_s$ , appears as a forcing term in the upper-layer mass equation. Other notation is fairly standard:  $\phi_1 = \rho_0^{-1} p_s$ ,  $\phi_2 = \phi_1 + g' \eta$ , where  $p_s$  is the surface pressure field,  $\eta$  is the interface height field, and  $g'$  is reduced gravity. Imposing a rigid lid, the total depth  $H = d_1 + d_2$  is constant, with layer depths  $d_1 = H_1 - \eta$  and  $d_2 = H_2 + \eta$ . The terms  $\mathbf{D}_1$  and  $\mathbf{D}_2$  represent dissipation for the upper and lower layers, respectively.

In all of the simulations reported below,  $H_1 = 1000$  m,  $H_2 = 3000$  m, and the Coriolis parameter is  $f = 7 \times 10^{-5} \text{ s}^{-1}$ . The reduced gravity is chosen such that the internal gravity wave speed is  $2 \text{ m s}^{-1}$ , yielding an internal deformation radius of about 28.6 km. We use a square doubly periodic domain with width  $L = 2000$  km resolved by 512 grid points in each direction. This gives a grid spacing of about  $dx = 3.9$  km, implying that the deformation radius is well resolved. Other parameters used in our simulations are shown in [Table 1](#).

### b. The slab layer

Two versions of the slab-layer model are considered. Version S1 neglects the self-advection of slab-layer momentum and version S2 attempts to retain it. Essentially, we consider that embedded near the top of the surface layer of our two-layer model is a boundary layer correction. Nonlinear Ekman theory assumes this correction to vary slowly in time and to obey a pressureless dynamics. That is, since the horizontal pressure gradient force is depth-independent in each of the two layers, it does not enter into the force balance of the boundary layer  $z$ -dependent horizontal velocity  $\mathbf{u}_s$ . In S1, terms quadratic in  $\mathbf{u}_s$  are neglected, and it is straightforward to integrate vertically to get a prognostic equation for the slab-layer transport,  $\mathbf{U}_s = \int \mathbf{u}_s dz$ . When quadratic terms in  $\mathbf{u}_s$  are kept, however, integrating vertically requires further assumptions. A simple

<sup>1</sup> It is interesting to note that Weller’s slab-layer approach drew on Stern’s (see chapter 8 of [Stern 1975](#)). While Stern’s focus was mainly on the nonlinear Ekman theory, he also considered particular solutions under oscillatory forcing and noted a singularity at the inertial frequency. Weller’s instability, by contrast, came from an examination of homogeneous solutions.

TABLE 1. The parameters used in our simulations.

	Parameters	Symbols	Values
BF, S1, and S2 simulations	Domain size	$L_x = L_y$	2000 km
	Number of grid points	$n_x = n_y$	512
	Time step	$\Delta t$	300 s
	Coriolis parameter	$f$	$7 \times 10^{-5} \text{ s}^{-1}$
	Amplitude of steady wind stress	$\tau_0$	$0.1 \text{ N m}^{-2}$
	Biharmonic horizontal viscosity coefficient	$A_{\text{bh}}$	$dx^4 \times 10^{-5} \text{ s}^{-1}$
	Bottom drag coefficient	$r_{\text{drag}}$	$10^{-7} \text{ s}^{-1}$
	Inverse Laplacian dissipation coefficient	$r_{\text{invLap}}$	$(2\pi/L_y)^2 \times 10^{-6} \text{ s}^{-1}$
	Slab-layer thickness	$H_s$	50 m
	Upper-layer thickness	$H_1$	1000 m
	Lower-layer thickness	$H_2$	3000 m
	Internal gravity wave speed	$c_{\text{bc}}$	$2 \text{ m s}^{-1}$
Simulations in <a href="#">appendix A</a>	Domain size	$L_x = L_y$	1000 km
	Number of grid points	$n_x = n_y$	512
	Time step	$\Delta t$	100 s
	Coriolis parameter	$f$	$7 \times 10^{-5} \text{ s}^{-1}$
	Amplitude of steady wind stress	$\tau_0$	$0.1 \text{ N m}^{-2}$
	Amplitude of unsteady wind stress	$\tau_1$	$10^{-3} \text{ N m}^{-2}$
	Biharmonic horizontal viscosity coefficient	$A_{\text{bh}}$	$dx^4 \times 10^{-5} \text{ s}^{-1}$
	Slab-layer thickness	$H_s$	50 m
	Maximum Rossby number of the prescribed flows	$\text{Ro}_{\text{max}}$	0.06

choice is to assume a depth-independent constant value of  $\mathbf{u}_s$ . The vertical integral of  $(\mathbf{u}_s \cdot \nabla)\mathbf{u}_s$  is then given by  $(1/H_s)(\mathbf{U}_s \cdot \nabla)\mathbf{U}_s$ , where  $H_s$  is an assumed slab-layer thickness.<sup>2</sup> The first version of the slab-layer model, S1, is given by

$$\frac{\partial}{\partial t} \mathbf{U}_s + (\mathbf{U}_s \cdot \nabla)\mathbf{u}_1 + (\mathbf{u}_1 \cdot \nabla)\mathbf{U}_s + f\hat{\mathbf{z}} \times \mathbf{U}_s = \frac{\boldsymbol{\tau}}{\rho_0} + \mathbf{D}_s,$$

and the second version, S2, is given by

$$\begin{aligned} \frac{\partial}{\partial t} \mathbf{U}_s + \frac{1}{H_s} (\mathbf{U}_s \cdot \nabla)\mathbf{U}_s + (\mathbf{U}_s \cdot \nabla)\mathbf{u}_1 + (\mathbf{u}_1 \cdot \nabla)\mathbf{U}_s \\ + f\hat{\mathbf{z}} \times \mathbf{U}_s = \frac{\boldsymbol{\tau}}{\rho_0} + \mathbf{D}_s. \end{aligned}$$

Here,  $\mathbf{D}_s$  is a dissipation term to be described below. To compare, the model in [Wenegrat and Thomas \(2017\)](#) corresponds to S1 rewritten in curvilinear coordinates and without the tendency and dissipation terms. S1 is also similar to slab-layer models such as those used by [Weller \(1982\)](#) and [Stern \(1975\)](#). Differences are that Weller dropped the  $(\mathbf{u}_1 \cdot \nabla)\mathbf{U}_s$  term following a scale analysis for the problem he considered, and Stern retained an additional term related to vertical advection of horizontal momentum [see Eq. (8) of [section 3d](#) below, and Eq. 8.2.20 of [Stern \(1975\)](#)]. Stern also considered a term similar to the self-advection of slab-layer momentum retained in S2, but then restricted attention to a regime in which it could be neglected.

<sup>2</sup> One might also consider a more general choice of the vertical structure  $\mathbf{u}_s(z)$ . In this case, the quadratic term will have a different vertical structure from the linear terms, and how one might proceed is discussed in [appendix B](#).

### c. Wind forcing

Forcing is by a zonal wind stress, the amplitude of which has steady and time-dependent components. That is,

$$\boldsymbol{\tau} = [\tau_0 + \tau_1(t)] \cos\left(\frac{2\pi y}{L}\right) \hat{\mathbf{x}}, \quad (2)$$

in which  $\tau_0 = 0.1 \text{ N m}^{-2}$  and  $\tau_1$  is normalized such that its RMS value is  $0.2\tau_0$  (with a maximum value of  $0.83\tau_0$ ). The steady winds excite baroclinically unstable jets which fuel an eddy-rich circulation. Transient forcing is similar to that used to excite near-inertial oscillations in [Taylor and Straub \(2015\)](#) and [Barkan et al. \(2017\)](#) and is meant as a very crude representation of synoptic time scale winds. A time series for  $\tau_1$  is constructed by combining 30 000 sinusoids with random phases and with periods linearly sampled between 0.1 and 3000 days. To be specific,

$$\tau_1(t) = \sum_{n=1}^{30000} A_n \sin(\omega_n t + \varphi_n), \quad (3)$$

where the  $\omega_n$  are frequencies, the  $\varphi_n$  are random phases, and the  $A_n$  are chosen so as to correspond to an Ornstein–Uhlenbeck process with a damping time scale of 5 days. Application of this time-dependent forcing to our model adds a robust field of near-inertial oscillations, which are free to interact with the geostrophic and Ekman flows excited by the steady winds.

### d. The dissipation terms

A biharmonic hyperviscosity is used to dissipate small-scale variance in both the slab-layer and two-layer models. The two-layer model also includes a linear bottom drag and an inverse Laplacian damping. The latter is applied to the barotropic mode and accounts for the bulk of energy dissipation in the two-layer model. In the forced-dissipative  $f$ -plane equilibrium solutions that

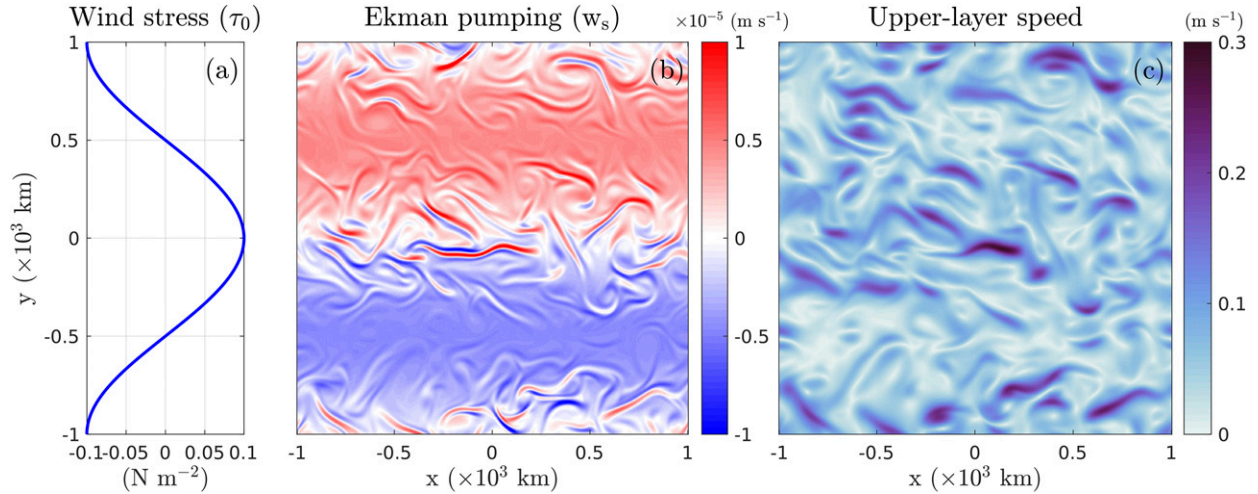


FIG. 1. S1 simulation with steady wind forcing. (a) Wind stress structure. (b) Pumping velocities. (c) Upper-layer speed.

we consider, a strong inverse energy cascade leads to a pile-up of energy near the largest available scales. The artificial inverse Laplacian dissipates preferentially at large scales and thus results in statistical equilibria that are not dominated by a small number of domain-filling eddies. Referring to (1), S1, and S2,

$$\begin{aligned} \mathbf{D}_s &= -A_{\text{bh}} \nabla^4 \mathbf{U}_s, \\ \mathbf{D}_1 &= r_{\text{invLap}} \nabla^{-2} \mathbf{u}_1 - A_{\text{bh}} \nabla^4 \mathbf{u}_1, \\ \mathbf{D}_2 &= r_{\text{invLap}} \nabla^{-2} \mathbf{u}_2 - A_{\text{bh}} \nabla^4 \mathbf{u}_2 - r_{\text{drag}} \mathbf{u}_2, \end{aligned} \quad (4)$$

with coefficients given by  $r_{\text{invLap}} = \kappa_0^2 \times 10^{-6} \text{ s}^{-1}$  and  $r_{\text{drag}} = 10^{-7} \text{ s}^{-1}$ , in which  $\kappa_0$  is the smallest horizontal wavenumber. The biharmonic viscosity coefficients are given by  $A_{\text{bh}} = dx^4 \times 10^{-5} \text{ s}^{-1}$  (in which  $dx$  is the grid spacing) for both the slab Ekman layer and the two interior layers. Other parameters are shown in Table 1.

### 3. Results

This section presents results from our two-layer model simulations. For steady forcing, equilibrium solutions are insensitive to whether forcing is applied using the S1 or S2 slab models or as a body force (BF). Spinups to equilibrium, however, are qualitatively different. Also qualitatively different are statistical equilibria when unsteady forcing is included. These differences are evident both in the slab layer and interior velocity fields, and are related to an instability in which near-inertial motion grows in the presence of convergent Ekman flow. We also comment on how these differences are reflected in the surface pressure field, as this is of interest in anticipation of the upcoming SWOT mission. Finally, we briefly consider how vertical advection—which was neglected in our slab-layer model equations—might be included.

#### a. Spinup under steady forcing

Sample snapshots of the pumping velocity  $w_s$  and upper-layer current speed  $|\mathbf{u}_1|$  for a simulation using S1 and steady

forcing are shown in Fig. 1. The pumping velocity shows both the wavenumber one pattern imposed by the forcing as well as smaller-scale structures related to the surface currents. These smaller-scale structures evolve on the time scales associated with the geostrophic turbulence (not shown). As will be shown below, forcing instead with S2 yields qualitatively similar results at statistical equilibrium.

The spinups, by contrast, are quite different depending on whether S1 or S2 is used. Forcing with S2 produces a strong north–south asymmetry between the cyclonic (northern) and anticyclonic (southern) regions of wind forcing. This is shown in Fig. 2, and is absent in S1 and BF simulations. Figures 2a and 2b present Hovmöller diagrams of  $w_s$  for a spinup from rest using S2. Figure 2a gives a blow-up of the first 150 days of this 2000-day spinup. Superposed on a steady wavenumber one pattern are near-inertial oscillations that grow in the southern part of the domain and decay in the north. Also evident is an interference pattern with a longer period of about 10 days. At around day 1200, baroclinic instability produces a rich eddy field. This serves to advect and eventually dissipate the near-inertial oscillations (see also selected snapshots in Figs. 2c–d). By  $t = 1600$  days, the asymmetry has disappeared in the S2 simulations, and the pumping velocity becomes qualitatively similar to that found using S1 (cf. Fig. 2e with Fig. 1b). Spinup of an analogous S1 simulation shows similar near-inertial oscillations, but with no asymmetry between the north and the south.

The initial instability can be understood in a relatively straightforward fashion. We consider the limit where  $\mathbf{U}_s$  is well approximated by the standard Ekman drift plus a weaker perturbation. For a zonal wind stress, this gives  $\mathbf{U}_s \approx V_{\text{Ek}} \hat{\mathbf{y}} + \mathbf{U}'$ , where  $V_{\text{Ek}} = -\tau^x / (\rho_0 f)$  is the large-scale Ekman transport and  $\mathbf{U}' = U' \hat{\mathbf{x}} + V' \hat{\mathbf{y}}$  is considered small by comparison. The leading-order pumping velocity is that given by linear Ekman theory, i.e.,  $w_{\text{Ek}} = (\partial/\partial y)V_{\text{Ek}}$ . To further simplify, the interior velocity is also assumed to be small ( $\mathbf{u}_1$  is small compared to  $\mathbf{U}'/H_s$ ), so that

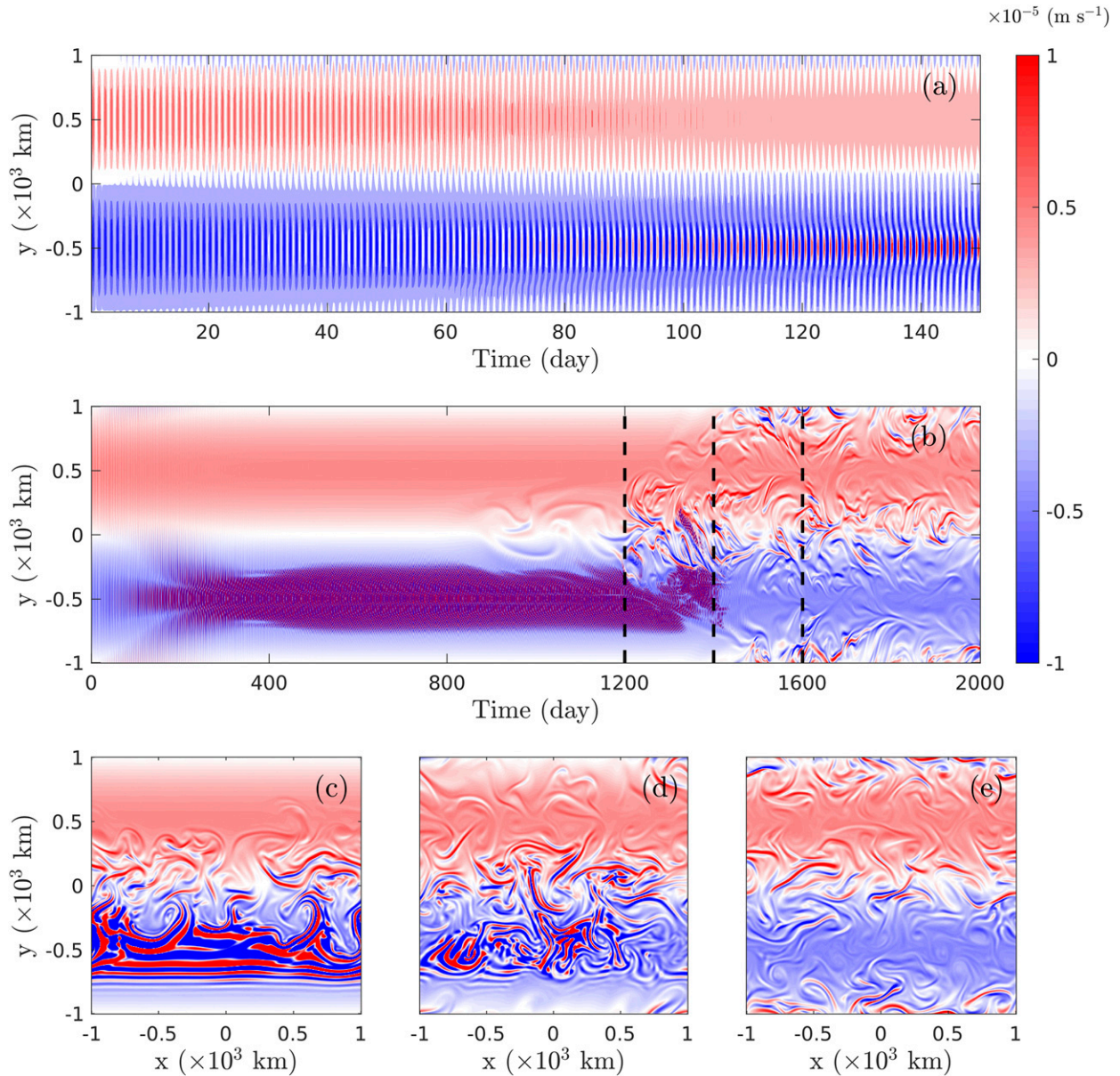


FIG. 2. Pumping velocities for a spinup under steady forcing using the S2 model. Hovmöller diagrams for (a) the first 150 days and (b) the full 2000 days of the simulation. (c)–(e) Snapshots at 1200, 1400, and 1600 days, as marked by dashed lines in (b).

perturbations to the S2 slab-layer momentum evolve according to

$$\begin{aligned} \frac{\partial}{\partial t} U' + \frac{V_{EK}}{H_s} \frac{\partial}{\partial y} U' &= fV', \\ \frac{\partial}{\partial t} V' + \frac{V_{EK}}{H_s} \frac{\partial}{\partial y} V' &= -fU' - \frac{w_{EK}}{H_s} V'. \end{aligned} \quad (5)$$

Referring back to Fig. 2, we note that the core of the instability occurs where  $V_{EK} = 0$ . Taking this to be the case (i.e., focusing on the latitude of maximum pumping), the two equations above can be combined to yield

$$V''_t + \sigma V'_t + f^2 V' = 0, \quad (6)$$

where  $\sigma = w_{EK}/H_s$ . Depending on the sign of the pumping, this describes either a damped or a growing harmonic oscillation. For  $\sigma$  small compared to  $f$ , (6) predicts near-inertial oscillations whose amplitude grows at rate  $-\sigma/2$ . In words, downwelling implies growth and the growth rate goes like the pumping velocity normalized by the slab-layer thickness.

The only significant difference between the above instability and that discussed by Weller is one of interpretation. In our case, the base state is defined as an Ekman flow, whereas in Weller's it was a geostrophic flow which included an order Rossby number divergence. Mathematically, the

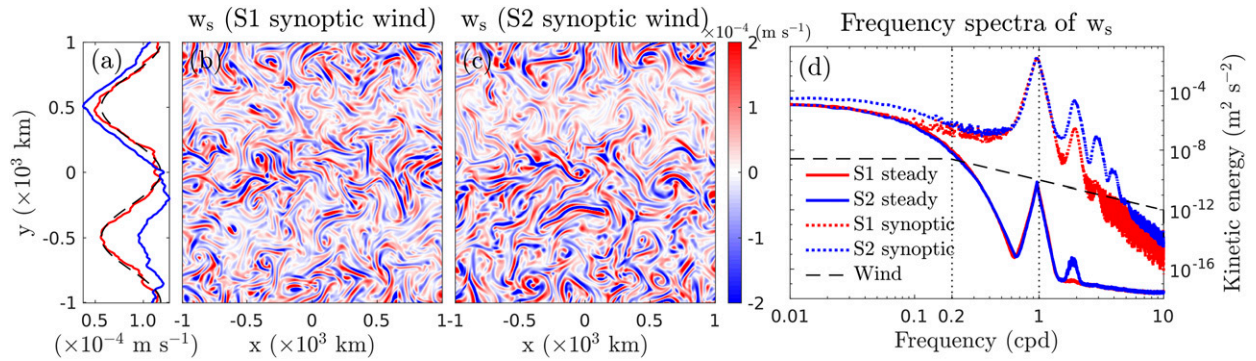


FIG. 3. Pumping velocities for the S1 and S2 models forced by a combination of steady and unsteady forcing. Shown are (a) zonally averaged RMS value of  $w_s$ , averaged over 300 days (red for S1, blue for S2 and dashed black for reference), (b) snapshot of S1, (c) snapshot of S2, and (d) frequency spectra of  $w_s$ . The dashed line in (d) illustrates the frequency spectrum of unsteady forcing, of which the high-frequency components start to decrease at 0.2 cycle per day (cpd).

two instabilities are equivalent (see Weller 1982, p. 1133). Klein and Treguer (1993) also derived an equation similar to (6), except that the damping or growth came from a spatial derivative, rather than from a time derivative as in our  $\sigma V'_t$  term [see their Eq. (19)]. They were examining a wind-forced reduced gravity model and found winds blowing across a geostrophic current to facilitate a collapse in horizontal scale of near-inertial motion. When the resulting waves propagated upwind, an instability was evident from the linear dispersion relation. Negatively damped harmonic oscillations in the context of geostrophic–NI interaction have also been discussed in detail by Whitt and Thomas (2015). The case they considered was similar to Weller in that the base state was meant to represent a geostrophic current. It was different in that horizontal divergence was assumed to vanish and the damping resulted from a Rayleigh drag term.

At later times the interior velocity,  $\mathbf{u}_1$ , can no longer be ignored and the dynamics becomes more complex until, eventually, any obvious asymmetry between the upwelling and downwelling regions is lost. We rationalize this disappearance by noting that advection terms involving  $\mathbf{u}_1$  can be expected to cascade variance in  $\mathbf{U}'$  toward small scales. Eventually, these more turbulent effects dominate over this relatively weak instability. In other words, the geostrophic turbulence transfers near-inertial variance in  $\mathbf{U}_s$  downscale faster than it can be produced by this instability mechanism. As we discuss below, however, with time-dependent forcing, strong asymmetry persists at statistical equilibrium.

### b. Equilibrium solutions under transient forcing

In this subsection we consider the effect of adding time-dependent forcing [see Eqs. (2) and (3)]. Snapshots and frequency spectra of the pumping velocity at statistical equilibrium are shown in Fig. 3. For both S1 and S2, transients are much stronger than was the case for steady forcing. For example, the wavenumber one structure that was clearly evident under steady forcing becomes difficult to discern. For S1, a strong near-inertial peak and weaker peak near  $2f$  are evident and low frequencies are unaffected. For S2, the increase in

amplitude (relative to steady forcing) includes both a near-inertial peak and a more broad banded response. In particular, peaks centered on integer multiples of  $f$  and an increased variance at low frequencies are evident. Peaks at multiples of  $f$  are more robust since in S2 these are readily excited by quadratic nonlinearity of slab-layer near-inertial modes, whereas in S1 they are instead excited by interactions between the slab layer and the weaker interior near-inertial flow.

Snapshots for the S2 simulation show a clear north–south asymmetry similar to that seen in the spinup with steady forcing. Under steady forcing, this asymmetry disappeared as geostrophic turbulence swept near-inertial variance downscale faster than it could be produced by the instability. Transient forcing serves to continuously seed the instability seen in the previous section. We can think of the northern and southern halves of the domain as similar to damped harmonic oscillators, but with positive damping in the north and negative damping in the south. Presumably it is this difference in the dynamics that produces the strong asymmetry seen in the Fig. 3c. That said, other nonlinearities present in S2 but absent in S1 that are not directly related to the instability may also be at play. For example, the large-scale (linear) Ekman drift acts to advect smaller scale features in the slab layer toward regions of downwelling. Additionally, the instability described above is a simplification in that slowly varying nonlinear Ekman divergence could also be considered part of the base state flow.

We next consider differences in the interior response to the different forcing prescriptions. Frequency spectra of kinetic energy are shown in Fig. 4. Upper- and lower-layer KE correspond to the variance of  $\mathbf{u}_1$  and  $\mathbf{u}_2$  and are not weighted by either  $H_{1,2}$  or  $d_{1,2}$ . Similarly, barotropic and baroclinic KE correspond to the variance of the two linear mode velocities:  $\mathbf{u}_{\text{BC}} = \mathbf{u}_2 - \mathbf{u}_1$  and  $\mathbf{u}_{\text{BT}} = (H_1 \mathbf{u}_1 + H_2 \mathbf{u}_2)/H$ . At low frequencies, differences among the three formulations are small. Comparing simulations forced using BF and S1, results are similar in the lower layer but differ in the upper layer (and therefore in projections onto the barotropic and baroclinic modes). These differences, however, can be made small by recalculating the spectra, but substituting  $\mathbf{u}'_1$  for  $\mathbf{u}_1$ , where the former is given by  $\mathbf{u}'_1 = \mathbf{u}_1 + \mathbf{U}_s/H_s$ . In other words, if one distributes the slab-layer

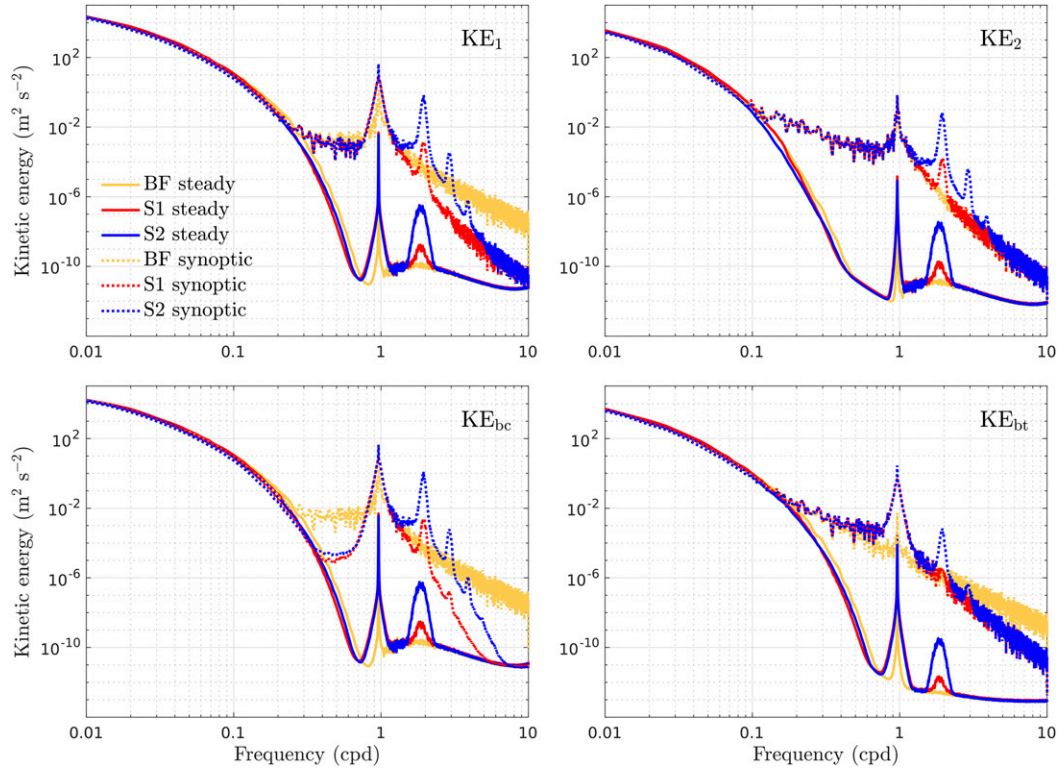


FIG. 4. Frequency spectra of kinetic energy for ( $KE_1$ ) the upper layer, ( $KE_2$ ) the lower layer, ( $KE_{bc}$ ) the linear baroclinic mode, and ( $KE_{bt}$ ) the barotropic mode.  $KE_1$  and  $KE_2$  correspond to the variance of  $\mathbf{u}_1$  and  $\mathbf{u}_2$  and are not weighted by layer thickness. Similarly,  $KE_{bt}$  and  $KE_{bc}$  correspond to velocity variance for the two linear modes, defined as  $\mathbf{u}_{bc} = \mathbf{u}_2 - \mathbf{u}_1$  and  $\mathbf{u}_{bt} = (H_1\mathbf{u}_1 + H_2\mathbf{u}_2)/H$ .

velocity over the upper layer, the S1 and BF forcings produce similar results. This suggests that differences between these two formulations have mainly to do with bookkeeping: the S1 formulation allows us to separate the total upper-layer velocity into slab-layer and interior components, but this separation has relatively little impact on the kinetic energy spectra. Differences between S2 and the other two forcing prescriptions are more substantial, with S2 showing increased superinertial energy in both layers.

That there is a near-inertial peak in the barotropic mode also deserves comment in that a stand-alone barotropic model does not admit inertial oscillations. Recall that we use a linear definition of the barotropic mode. Since it is the vertically integrated transport (and not its linear approximation) that must be nondivergent, there is an implied horizontal divergence in  $\mathbf{u}_{BT}$ . Specifically, its divergence must cancel that of  $\eta\mathbf{u}_{BC} + \mathbf{U}_s$ . That is, it is the divergence of  $(H_1 - \eta)\mathbf{u}_1 + (H_2 + \eta)\mathbf{u}_2 + \mathbf{U}_s$ , or, equivalently, of  $H\mathbf{u}_{BT} + \eta\mathbf{u}_{BC} + \mathbf{U}_s$  which must vanish. Since both  $\mathbf{u}_{BC}$  and  $\mathbf{U}_s$  include divergence at near-inertial time scales, so then must  $\mathbf{u}_{BT}$ . The inertial peak in the barotropic mode is considerably stronger for S1 than for BF forcing (bottom-right panel of Fig. 4), which indicates that  $\mathbf{U}_s$  dominates over  $\eta\mathbf{u}_{BC}$ . Spectra for the S2 case are similar to S1, except for an additional peak near  $2f$ .

Recall from Fig. 3 that transient S2 forcing produces pumping velocities that have both an increased low-frequency

signature and a  $2f$  peak (see dashed blue curve in Fig. 3d). This is a consequence of the quadratic nonlinearity kept in S2, but filtered in S1. In other words, quadratic nonlinearity of near-inertial motion projects onto both low frequencies and to frequencies close to  $2f$ . This additional low-frequency pumping does not, however, seem to excite a large interior response. For example, little difference between KE spectra is seen between the S1 and S2 cases in Fig. 4. We are nonetheless curious as to whether the added low-frequency pumping in our S2 simulation might impact the low-frequency dynamics in some other significant way. One possibility is that the low-frequency  $w_s$  might provide a significant energy source or sink to the balanced flow. To assess this, recall that the wind power input to quasigeostrophic flows can be interpreted as an area integral and time average of the pumping velocity multiplied by the upper-layer streamfunction.<sup>3</sup> In our simulations, this is equivalent to the low-passed pumping velocity multiplied by a low-passed version of surface pressure. We calculated this and found a correlation that was consistent with an energy sink (not

<sup>3</sup>That is, multiplying the quasigeostrophic potential vorticity equation by the streamfunction,  $\psi$ , and integrating by parts yields the energy equation (Pedlosky 1987). Since  $w_s$  appears as a forcing term in the potential vorticity equation,  $\psi w_s$  or, equivalently,  $\eta w_s$  appears as a forcing term for the energy.

shown). This sink of balanced energy, however, was small compared to the sink related to the artificial removal of energy by the inverse Laplacian dissipation. Because the principal energy sink is artificial, we did not pursue this analysis further.

### c. Projections onto surface pressure

In the context of the upcoming SWOT satellite altimetry mission, it is interesting to consider how the high-frequency signals seen in the three models project onto surface pressure. SWOT will measure sea surface height at horizontal scales near the mesoscale–submesoscale transition and there is interest in decomposing the signal into balanced and unbalanced components (Torres et al. 2018). Our model uses a rigid lid, and we take pressure on the lid as the model equivalent of sea surface height. In the S1 and S2 slab models,  $\mathbf{U}_s$  is pressureless by design. As such, surface pressure must be related to the interior velocity field, e.g., to  $\mathbf{u}_{BT}$  and  $\mathbf{u}_{BC}$ .

The baroclinic mode can be further decomposed into geostrophic and ageostrophic contributions using the well-known linear mode decomposition (e.g., Salmon 1998). Recognizing that the linear (quasigeostrophic) potential vorticity is zero for Poincaré waves, we can define a streamfunction for the geostrophic part of the baroclinic flow by

$$\nabla^2 \psi - \frac{f^2}{gH_{\text{eff}}} \psi = \zeta_{\text{BC}} - \frac{f}{H_{\text{eff}}} \eta, \quad (7)$$

where  $\zeta_{\text{BC}}$  is baroclinic relative vorticity and  $H_{\text{eff}} = H_1 H_2 / H$ . Applying geostrophy relates  $\psi$  to the interface height field  $\eta$ . Given  $\psi$ , one can then infer the portion of the  $\eta$  field that is associated with the geostrophic part of the baroclinic flow. The residual is related to ageostrophic modes. Then, since surface pressure is negatively proportional to  $\eta$  for a baroclinic mode, it is straightforward to decompose the surface pressure field into three parts: one related to the barotropic mode and two related, respectively, to geostrophic and ageostrophic parts of the baroclinic mode.

Using this methodology, we decomposed high-passed snapshots of the S1, S2, and BF simulations to infer the high-passed surface pressure and its projections onto the geostrophic and ageostrophic parts of the baroclinic mode. The high-pass filter was defined as a weighted average over an 8-day window, with the weighting function defined by a Gaussian with a 1.2-day time scale and centered in the window. Results are shown in Fig. 5 and the contrast among the three cases is striking. For BF forcing, high-passed surface pressure is dominated by fast time scale baroclinic “geostrophic” modes. For S1, geostrophic and ageostrophic contributions are more comparable (and, curiously, show a large degree of cancellation) and for S2, ageostrophic modes are larger, especially at small scales. The point we wish to emphasize here is not so much the detailed differences of these three cases, but simply that unbalanced contributions to surface pressure appear sensitive to how surface-layer dynamics is represented. In more complete models, for example, high-frequency contributions to sea surface height will likely be sensitive to resolution and parameterization choices.

### d. Vertical advection terms

In deriving our slab models, vertical advection of slab-layer momentum was neglected. That is,  $w_1 \partial_z \mathbf{u}_s$  and  $w_s \partial_z \mathbf{u}_s$  terms are not accounted for in S1 and S2. We first consider vertical advection of slab-layer momentum by the interior vertical velocity, i.e., the  $w_1 \partial_z \mathbf{u}_s$  term. This can be dealt with in a straightforward manner by noting that  $w_1 = -z(\nabla \cdot \mathbf{u}_1)$  and integrating by parts over the surface layer to obtain

$$\int w_1 \frac{\partial}{\partial z} \mathbf{u}_s dz = (\nabla \cdot \mathbf{u}_1) \mathbf{U}_s. \quad (8)$$

Accounting for the  $w_s \partial_z \mathbf{u}_s$  term is less straightforward, but leads to a similar expression. Specifically, we find

$$\int w_s \frac{\partial}{\partial z} \mathbf{u}_s dz = \frac{1}{2H_s} (\nabla \cdot \mathbf{U}_s) \mathbf{U}_s. \quad (9)$$

The coefficient  $1/(2H_s)$  is similar to the  $1/H_s$  seen for the advective term in S2. Here, an additional factor of 1/2 appears, as is discussed in appendix B.

Including the  $(\nabla \cdot \mathbf{u}_1) \mathbf{U}_s$  term in our S1 or S2 simulations does not lead to any noticeable differences; however, including a  $(1/2H_s)(\nabla \cdot \mathbf{U}_s) \mathbf{U}_s$  term in our S2 simulations does. Essentially, this term serves to exacerbate differences between S1 and S2. For example, growth rates in the instability described by  $\sigma$  [see (6)] are faster by a factor of 2 when the additional term is included. This, in turn, leads to increased asymmetries between the northern and southern parts of our domain in simulations forced with unsteady winds. The effect of adding this vertical advection term is qualitatively similar to that of reducing  $H_s$ . This is evident from Fig. 6, which shows snapshots of  $w_s$  for four simulations, with and without the vertical advection term and for different choices of  $H_s$ . Forcing is similar to that used in our transient forcing simulations above. Neglecting the vertical advection term and taking  $H_s = 25$  m gives results that are qualitatively similar to retaining the vertical advection term and taking  $H_s = 50$  m. Similarly, retaining vertical advection and using  $H_s = 100$  m gives results similar to neglecting vertical advection and taking  $H_s = 50$  m.

## 4. Conclusions

We used different slab-layer models to represent nonlinear Ekman flows and surface-layer near-inertial oscillations, and coupled these slab layers to a two-layer shallow water model. Our original motivation was to see what impacts these modeling choices might have on geostrophic turbulence excited by wind forcing. In particular, Wenegrat and Thomas (2017) pointed out that the nonlinear Ekman equations produced interesting features in curvilinear flows. These and other modifications to linear Ekman theory can be large and have been shown, for example, to influence vertical nutrient transport, affecting biological productivity and carbon uptake (e.g., Mahadevan et al. 2008; Mahadevan 2016). We did not find that embedding a slab layer in our two-layer model had an obvious impact on the low-frequency portion of the interior (two-layer) flow. It did, however, strongly impact the high frequencies. Other main conclusions are as follows:

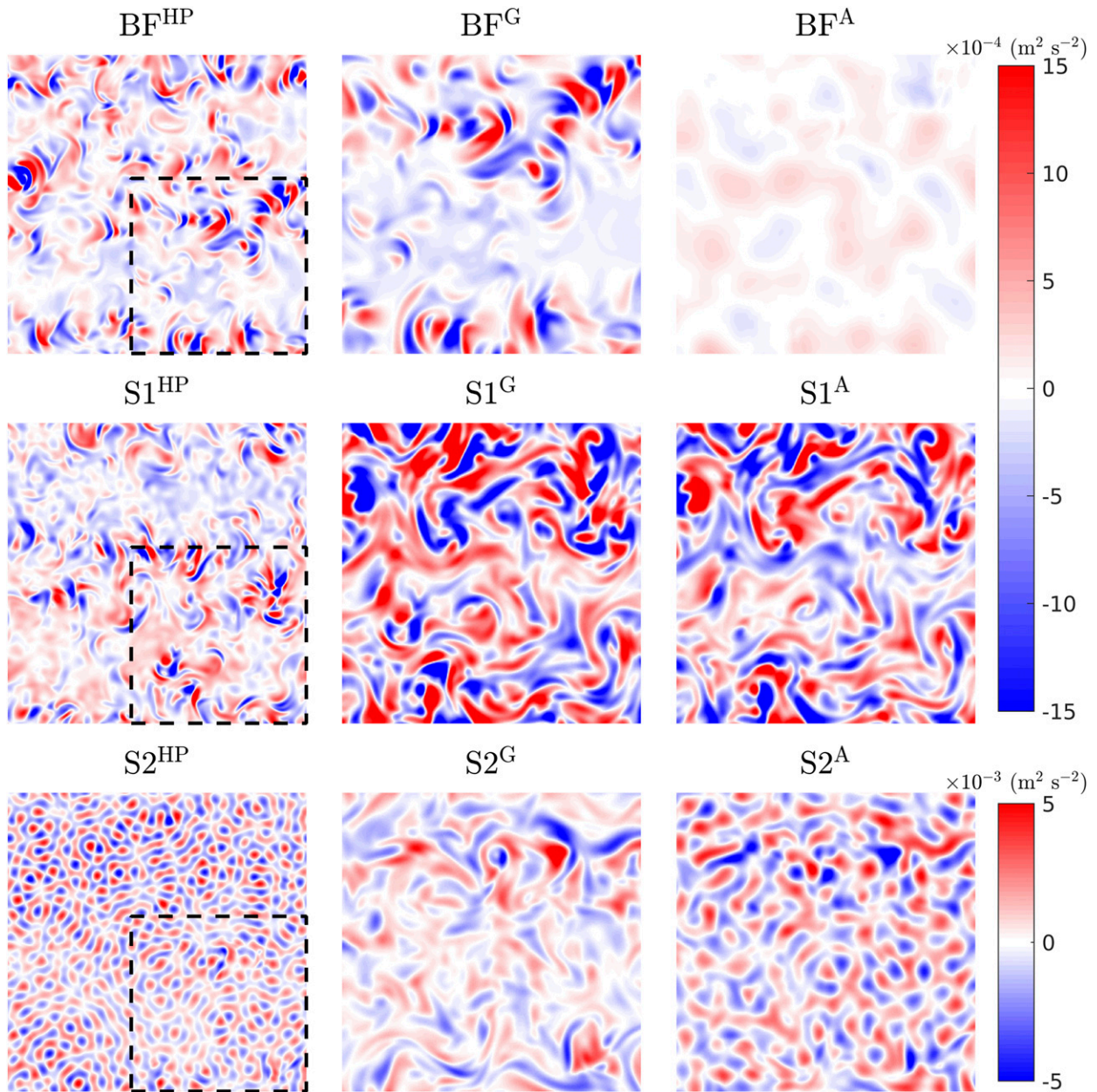


FIG. 5. High-passed pressure fields in BF, S1, and S2 simulations using a combination of steady and unsteady winds. (left) Total high-passed pressure, (center) geostrophic component, and (right) ageostrophic component. Note that the center and right panels are blow-ups of the subdomain indicated by the dashed lines on the left panels. The barotropic component was considered geostrophic. It is included in the center panel fields and is small.

- 1) Allowing for self-advection of slab-layer momentum leads to a strong asymmetry between regions of large-scale cyclonic and anticyclonic forcing. This asymmetry arises as the result of a new instability [which can be thought of as a reinterpretation of the well-known instability described by [Weller \(1982\)](#)]. It is distinct from inertial or symmetric instability in which growth is related to anticyclonic vorticity in background flow. Instead, here it is the sign of the forcing that matters. In our S2 simulations, effects of the instability are evident
  - (i) in spinups under steady forcing, and
  - (ii) at equilibrium when transient forcing is added.
- 2) Interactions between near-inertial and Ekman-like flows in our S2 slab model are two-way. For example, transient forcing leads to both increased high- and low-frequency variance of pumping velocities. We interpret the latter as a transfer from high-to-low frequencies via quadratic nonlinearity in the slab-layer equation.
- 3) Differences of the interior kinetic energy spectra between simulations forced using our S1 and S2 versions of the slab

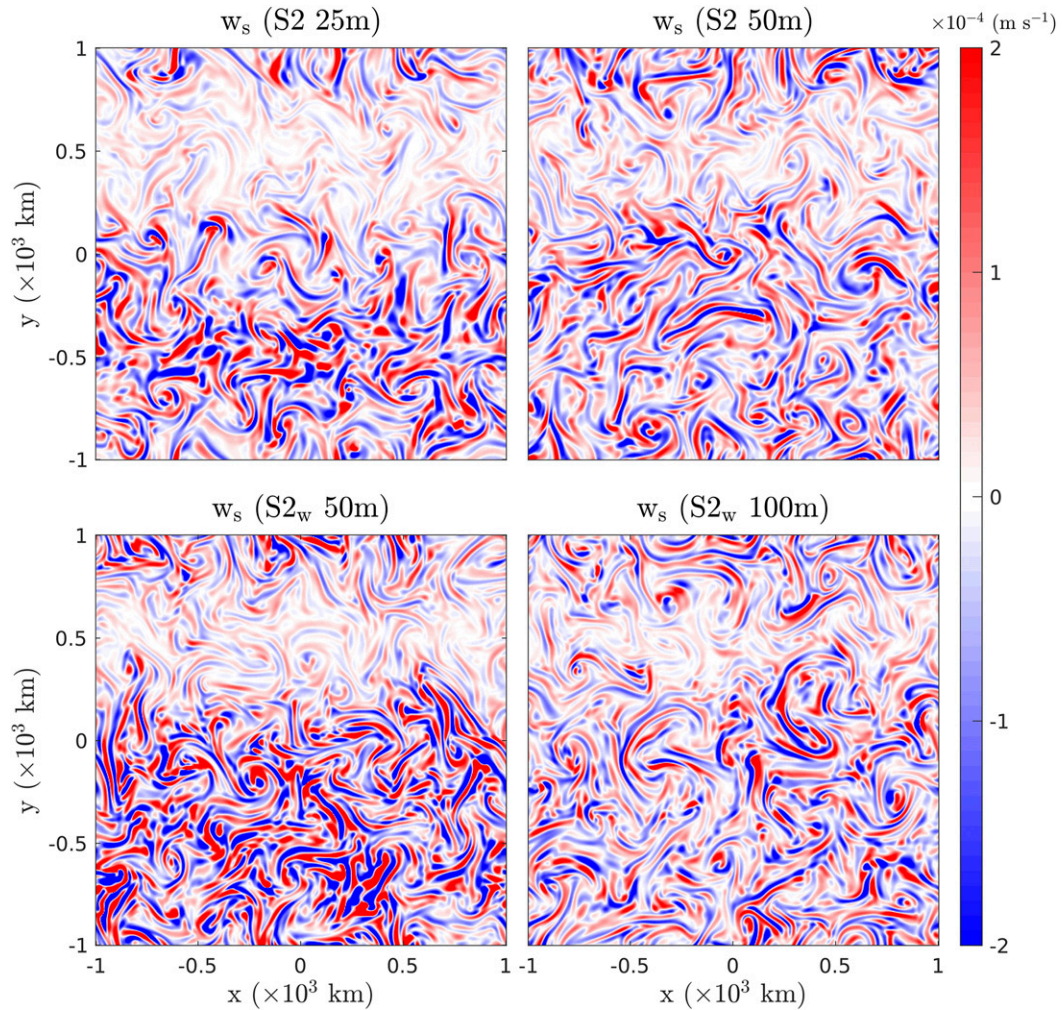


FIG. 6. Influence of the vertical advection terms in S2 simulations with a combination of steady and unsteady winds. Upper panels are pumping velocities without vertical advection using  $H_s = [25 \text{ m}, 50 \text{ m}]$ , and lower panels are pumping velocities with vertical advection using  $H_s = [50 \text{ m}, 100 \text{ m}]$ .

model are largely confined to high frequencies. The increased low-frequency pumping in our S2 simulations does not produce an obvious low-frequency response in the interior flow.

- 4) The different modeling choices considered lead to large differences in high-frequency components of the flow. Although the size of these differences (cf. Fig. 5) is surely an artifact of the simplicity of our model, the results nonetheless suggest that the details of how the upper ocean is represented will lead to differences in wind-driven unbalanced flow, including how it projects onto sea surface height.

The coupled model we developed omits horizontal propagation of surface-layer near-inertial waves and does not account for vertical structure in the slab-layer flow. It will therefore be interesting to test the robustness of our results in a more complete setting. In particular, we wish to test whether the instability found using S2 has a counterpart in general circulation models that vertically resolve the surface layer. In a

related study, we use large-eddy simulations to show that the Boussinesq equations do indeed admit an instability similar to the one described here (K. Duquette et al. 2020, unpublished manuscript).

Also interesting will be to consider Ekman–NI interaction in simulations that (i) allow for wave propagation and (ii) take into account dependence of wind stress on ocean current velocities. Allowing for surface velocity effects, one anticipates anticyclonic forcing over cyclones and cyclonic forcing over anticyclones (Duhaut and Straub 2006). That is, one expects increased convergence of the (linear) Ekman flow over cyclonic eddies and increased divergence over anticyclonic eddies. Because inertia–gravity waves quickly propagate out of cyclones, the increased convergence over anticyclones will likely be more significant. In other words, the decay version of the instability we describe may prove important over anticyclones, where it could supplement vertical wave propagation to provide an additional mechanism for removing near-inertial energy from the surface layer.

Finally, YBJ-type models such as that used by Asselin and Young (2020) typically side-step direct representation of the Ekman layer, e.g., by assuming near-inertial motion to be added impulsively at some initial time. As pointed out here, and by Wenegrat and Thomas (2017), nonlinear Ekman flows are complex and cannot be inferred from a spatially local knowledge of the surface velocity and wind stress. In our model, they obey a pressureless dynamics and therefore cannot be represented by balance relations such as quasi-geostrophy. YBJ models typically use a modified version of quasi-geostrophy to represent the low-frequency part of the total motion (although Xie and Vanneste (2015) pointed out that other choices might be possible). For these models to capture the total low-frequency flow—including both geostrophic and nonlinear Ekman components—may require a more appropriate balance law. Given such a law, presumably nonlinear Ekman flows could be incorporated by simply adding vertical viscosity to the equations and choosing appropriate boundary conditions for the elliptic inversion. This would allow these models to include effects such as those we discuss here.

*Acknowledgments.* We thank two anonymous reviewers for offering comments and criticisms that led to considerable improvements in the manuscript, and we gratefully acknowledge support from FRQNT and NSERC and the CSA.

### APPENDIX A

#### Slab Layer Results for Simple Specified Flows

Here we compare the S1 and S2 versions of the slab model in a stand-alone configuration. Specifically, we consider their response to a uniform wind stress blowing over a horizontally nondivergent circular eddy (described by a Gaussian streamfunction and such that the Rossby number,  $|\xi|/f$ , is about 0.06). The wind stress  $\tau$  is uniform in the  $\hat{x}$  direction, and produces a leading-order southward Ekman transport of about  $1.4 \text{ m}^2 \text{ s}^{-1}$ . Results at steady state are similar to those described by Wenegrat and Thomas (2017, see their Fig. 3), who used a similar setup. That is, nonlinear Ekman effects produce divergent zones on the northern and southern sides of the eddy, with the sign dependent on the vortex polarity.

The S1 and S2 models produce similar results in the long time limit. They both also produce fast time scale transients, which are robust, long-lived and different between the two models. The transients are evident even in simulations for which the forcing is ramped up over several inertial periods. Sample snapshots of the pumping are shown in Fig. A1. In the S1 simulations, the transients appear as clockwise whirling rings confined to the eddy, whereas in the S2 simulations these rings are pushed away by the leading-order southward Ekman drift. Animations of these simulations also show other differences between cyclones and anticyclones. For example, in the cyclones, phase propagation is outward near the center and inward on the periphery, whereas these signs are reversed in anticyclones.

We also considered solutions forced by a combination of steady and oscillatory winds. Specifically, forcing takes the

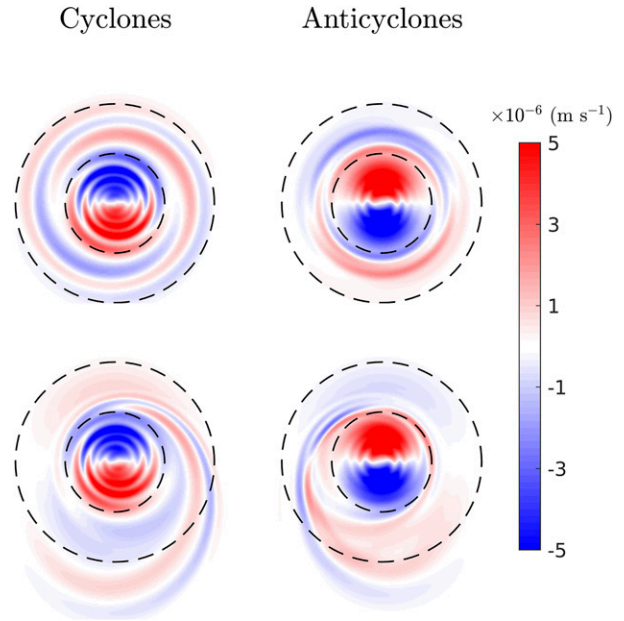


FIG. A1. Pumping velocities in slab models with prescribed circular vortices forced by steady wind stress for (top row) the S1 model and (bottom row) the S2 model. The vortices are described by a Gaussian streamfunction with an 80 km decay scale. Shown is a subdomain centered on the vortices with dashed lines corresponding to circles with radii of 100 and 200 km.

form of a spatially uniform, oscillating eastward stress with  $\tau_x = \tau_0 + \tau_1 \sin(\omega t)$ . The two panels in Fig. A2 show frequency spectra of pumping velocities in the S1 model with different choices of the forcing frequency  $\omega$ . Spectra were calculated using output between 50 and 100 inertial periods following application of the oscillatory forcing. Unsurprisingly, the response shows a peak at the forcing frequency. Notice also the presence of a secondary peak on the flank of the main inertial peak corresponding to the relative vorticity of the eddy. Less obvious is that peaks near the inertial frequency persist even when the forcing is off-inertial. These near-inertial peaks, however, get weaker as the forcing becomes more off-resonant. They also become weaker if a later time window is used to do the analysis. That is, they result from a homogeneous part of the solution needed to satisfy initial conditions. This homogeneous part decays, albeit slowly, in time.

### APPENDIX B

#### Computation of the Projection Coefficients

The projection coefficient  $1/(2H_s)$  in Eq. (9) is a factor of 2 smaller than similar coefficients in S2. To understand this difference, we assume that  $\mathbf{u}_s$  has some known vertical structure  $a(z)$ . Consistent with previous assumptions, we take

$$a = 1, \quad z > -H_s,$$

$$a = 0.5, \quad z = -H_s,$$

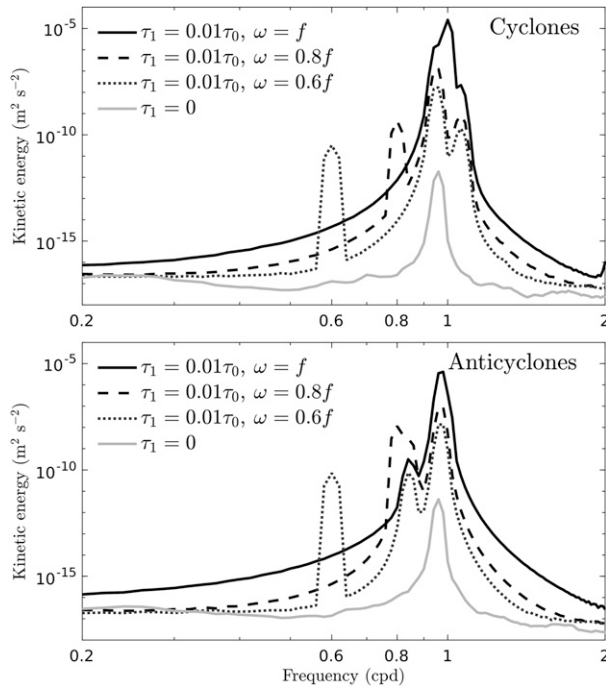


FIG. A2. Frequency spectra of pumping velocities for a combination of steady and unsteady forcing in the S1 model. Results are shown for different choices of near-inertial forcing (with the grey solid line giving a reference without unsteady forcing). The inertial peaks in the figure correspond to the peaks with frequencies nearby 1 cpd.

$$a = 0, \quad z < -H_s, \quad (\text{B1})$$

where the factor of  $1/2$  at  $z = -H_s$  is motivated by the Fourier representation of a series of opposite-signed step functions. For this choice of  $a(z)$ ,  $\partial_z \mathbf{u}_s$  is zero in the slab layer but has a delta function contribution at the base of the slab layer. That is,  $\partial_z \mathbf{u}_s = \delta(z + H_s) \mathbf{U}_s / H_s$ . Since  $w_s = \nabla \cdot \mathbf{U}_s$  at this depth, one concludes that

$$w_s \partial_z \mathbf{u}_s = (\nabla \cdot \mathbf{U}_s) \frac{\delta(z + H_s) \mathbf{U}_s}{H_s}. \quad (\text{B2})$$

We wish to project this delta function of  $z$  onto  $a(z)$ . In general, the projection of a function  $b(z)$  onto  $a$  is given by

$$\text{Proj}_{b \rightarrow a} = \frac{\int a(z)b(z) dz}{\int a^2(z) dz}, \quad (\text{B3})$$

where the integral extends over all  $z < 0$ . Taking  $b(z) = (1/H_s)(\nabla \cdot \mathbf{U}_s)\delta(z + H_s)\mathbf{U}_s$  gives  $\text{Proj}_{b \rightarrow a} = (1/2H_s)(\nabla \cdot \mathbf{U}_s)\mathbf{U}_s$ , consistent with (9).

The factor of  $1/2$  above may vary depending on the structure of  $a(z)$ . We also considered using an exponential profile to define  $a(z)$ . For this case, a similar procedure is also used for the  $(\mathbf{u}_s \cdot \nabla)\mathbf{u}_s$  term. That is, the vertical integral of this term is taken to be  $\gamma(\mathbf{U}_s \cdot \nabla)\mathbf{U}_s$ , where  $\gamma$  is a projection coefficient

found by projecting the vertical structure of  $a^2(z)$  back onto that of  $a$ . This leads to a similar result to that reported above. Specifically, the factor multiplying  $(\mathbf{U}_s \cdot \nabla)\mathbf{U}_s$  in S2 is twice as large as the factor multiplying the  $(\nabla \cdot \mathbf{U}_s)\mathbf{U}_s$  term.

Finally, one could argue that this factor of  $0.5$  should also appear in (8). In other words, (8) was obtained using a straightforward integral over the slab layer. If we were instead to assume a vertical structure and project that vertical structure back onto  $a$  prior to integrating, then a projection factor similar to that in (9) would appear. As noted in the text, however, this term has little obvious impact on our results and the projection coefficient was taken to be unity, as in (8) in our simulations.

## REFERENCES

- Alford, M. H., 2001: Internal swell generation: The spatial distribution of energy flux from the wind to mixed layer near-inertial motions. *J. Phys. Oceanogr.*, **31**, 2359–2368, [https://doi.org/10.1175/1520-0485\(2001\)031<2359:ISGTSD>2.0.CO;2](https://doi.org/10.1175/1520-0485(2001)031<2359:ISGTSD>2.0.CO;2).
- , 2003: Improved global maps and 54-year history of wind-work on ocean inertial motions. *Geophys. Res. Lett.*, **30**, 1424, <https://doi.org/10.1029/2002GL016614>.
- Asselin, O., and W. R. Young, 2020: Penetration of wind-generated near-inertial waves into a turbulent ocean. *J. Phys. Oceanogr.*, **50**, 1699–1716, <https://doi.org/10.1175/JPO-D-19-0319.1>.
- Barkan, R., K. B. Winters, and J. C. McWilliams, 2017: Stimulated imbalance and the enhancement of eddy kinetic energy dissipation by internal waves. *J. Phys. Oceanogr.*, **47**, 181–198, <https://doi.org/10.1175/JPO-D-16-0117.1>.
- Chelton, D., and S.-P. Xie, 2010: Coupled ocean-atmosphere interaction at oceanic mesoscales. *Oceanography*, **23**, 52–69, <https://doi.org/10.5670/oceanog.2010.05>.
- D’Asaro, E. A., 1985: The energy flux from the wind to near-inertial motions in the surface mixed layer. *J. Phys. Oceanogr.*, **15**, 1043–1059, [https://doi.org/10.1175/1520-0485\(1985\)015<1043:TEFFTW>2.0.CO;2](https://doi.org/10.1175/1520-0485(1985)015<1043:TEFFTW>2.0.CO;2).
- , 1989: The decay of wind-forced mixed layer inertial oscillations due to the  $\beta$  effect. *J. Geophys. Res.*, **94**, 2045–2056, <https://doi.org/10.1029/JC094iC02p02045>.
- Dawe, J. T., and L. Thompson, 2006: Effect of ocean surface currents on wind stress, heat flux, and wind power input to the ocean. *Geophys. Res. Lett.*, **33**, L09604, <https://doi.org/10.1029/2006GL025784>.
- Duhaut, T. H. A., and D. N. Straub, 2006: Wind stress dependence on ocean surface velocity: Implications for mechanical energy input to ocean circulation. *J. Phys. Oceanogr.*, **36**, 202–211, <https://doi.org/10.1175/JPO2842.1>.
- Elipot, S., R. Lumpkin, and G. Prieto, 2010: Modification of inertial oscillations by the mesoscale eddy field. *J. Geophys. Res.*, **115**, C09010, <https://doi.org/10.1029/2009JC005679>.
- Gaube, P., D. B. Chelton, R. M. Samelson, M. G. Schlax, and L. W. O’Neill, 2015: Satellite observations of mesoscale eddy-induced Ekman pumping. *J. Phys. Oceanogr.*, **45**, 104–132, <https://doi.org/10.1175/JPO-D-14-0032.1>.
- Gaultier, L., C. Ubelmann, and L.-L. Fu, 2016: The challenge of using future SWOT data for oceanic field reconstruction. *J. Atmos. Oceanic Technol.*, **33**, 119–126, <https://doi.org/10.1175/JTECH-D-15-0160.1>.
- Gill, A. E., 1984: On the behavior of internal waves in the wakes of storms. *J. Phys. Oceanogr.*, **14**, 1129–1151, [https://doi.org/10.1175/1520-0485\(1984\)014<1129:OTBOIW>2.0.CO;2](https://doi.org/10.1175/1520-0485(1984)014<1129:OTBOIW>2.0.CO;2).

- Grooms, I., and L.-P. Nadeau, 2016: The effects of mesoscale ocean–atmosphere coupling on the quasigeostrophic double gyre. *Fluids*, **1**, 34, <https://doi.org/10.3390/fluids1040034>.
- Hart, J. E., 2000: A note on nonlinear corrections to the Ekman layer pumping velocity. *Phys. Fluids*, **12**, 131–135, <https://doi.org/10.1063/1.870300>.
- Jing, Z., L. Wu, and X. Ma, 2017: Energy exchange between the mesoscale oceanic eddies and wind-forced near-inertial oscillations. *J. Phys. Oceanogr.*, **47**, 721–733, <https://doi.org/10.1175/JPO-D-16-0214.1>.
- Klein, P., and B. L. Hua, 1988: Mesoscale heterogeneity of the wind-driven mixed layer: Influence of a quasigeostrophic flow. *J. Mar. Res.*, **46**, 495–525, <https://doi.org/10.1357/002224088785113568>.
- , and A. M. Treguier, 1993: Inertial resonance induced by an oceanic jet. *J. Phys. Oceanogr.*, **23**, 1897–1915, [https://doi.org/10.1175/1520-0485\(1993\)023<1897:IRIBAO>2.0.CO;2](https://doi.org/10.1175/1520-0485(1993)023<1897:IRIBAO>2.0.CO;2).
- Kunze, E., 1985: Near-inertial wave propagation in geostrophic shear. *J. Phys. Oceanogr.*, **15**, 544–565, [https://doi.org/10.1175/1520-0485\(1985\)015<0544:NIWPIG>2.0.CO;2](https://doi.org/10.1175/1520-0485(1985)015<0544:NIWPIG>2.0.CO;2).
- Lee, D.-K., P. Niiler, A. Warn-Varnas, and S. Piasek, 1994: Wind-driven secondary circulation in ocean mesoscale. *J. Mar. Res.*, **52**, 371–396, <https://doi.org/10.1357/0022240943077037>.
- Mahadevan, A., 2016: The impact of submesoscale physics on primary productivity of plankton. *Annu. Rev. Mar. Sci.*, **8**, 161–184, <https://doi.org/10.1146/annurev-marine-010814-015912>.
- , L. N. Thomas, and A. Tandon, 2008: Comment on “Eddy/wind interactions stimulate extraordinary mid-ocean plankton blooms.” *Science*, **320**, 448, <https://doi.org/10.1126/science.1152111>.
- McGillcuddy, D. J., and Coauthors, 2007: Eddy/wind interactions stimulate extraordinary mid-ocean plankton blooms. *Science*, **316**, 1021–1026, <https://doi.org/10.1126/science.1136256>.
- , J. R. Ledwell, and L. A. Anderson, 2008: Response to comment on “Eddy/wind interactions stimulate extraordinary mid-ocean plankton blooms.” *Science*, **320**, 448, <https://doi.org/10.1126/science.1148974>.
- Morrow, R., and Coauthors, 2019: Global observations of fine-scale ocean surface topography with the Surface Water and Ocean Topography (SWOT) mission. *Front. Mar. Sci.*, **6**, 232, <https://doi.org/10.3389/fmars.2019.00232>.
- Niiler, P. P., 1969: On the Ekman divergence in an oceanic jet. *J. Geophys. Res.*, **74**, 7048–7052, <https://doi.org/10.1029/JC074i028p07048>.
- O’Neill, L. W., D. B. Chelton, and S. K. Esbensen, 2012: Covariability of surface wind and stress responses to sea surface temperature fronts. *J. Climate*, **25**, 5916–5942, <https://doi.org/10.1175/JCLI-D-11-00230.1>.
- Pedlosky, J., 1987: *Geophysical Fluid Dynamics*. Springer, 728 pp.
- , 2008: On the weakly nonlinear Ekman layer: Thickness and flux. *J. Phys. Oceanogr.*, **38**, 1334–1339, <https://doi.org/10.1175/2007JPO3830.1>.
- Perkins, H., 1976: Observed effect of an eddy on inertial oscillations. *Deep-Sea Res. Oceanogr. Abstr.*, **23**, 1037–1042, [https://doi.org/10.1016/0011-7471\(76\)90879-2](https://doi.org/10.1016/0011-7471(76)90879-2).
- Rocha, C. B., G. L. Wagner, and W. R. Young, 2018: Stimulated generation: Extraction of energy from balanced flow by near-inertial waves. *J. Fluid Mech.*, **847**, 417–451, <https://doi.org/10.1017/jfm.2018.308>.
- Salmon, R., 1998: *Lectures on Geophysical Fluid Dynamics*. Oxford University Press, 378 pp.
- Small, R., and Coauthors, 2008: Air-sea interaction over ocean fronts and eddies. *Dyn. Atmos. Oceans*, **45**, 274–319, <https://doi.org/10.1016/j.dynatmoce.2008.01.001>.
- Stern, M. E., 1975: *Ocean Circulation Physics*. Academic Press, 246 pp.
- , 1965: Interaction of a uniform wind stress with a geostrophic vortex. *Deep-Sea Res. Oceanogr. Abstr.*, **12**, 355–367, [https://doi.org/10.1016/0011-7471\(65\)90007-0](https://doi.org/10.1016/0011-7471(65)90007-0).
- Taylor, S., and D. Straub, 2015: Forced near-inertial motion and dissipation of low-frequency kinetic energy in a wind-driven channel flow. *J. Phys. Oceanogr.*, **46**, 79–93, <https://doi.org/10.1175/JPO-D-15-0060.1>.
- Thomas, L. N., and P. B. Rhines, 2002: Nonlinear stratified spin-up. *J. Fluid Mech.*, **473**, 211–244, <https://doi.org/10.1017/S0022112002002367>.
- Torres, H. S., P. Klein, D. Menemenlis, B. Qiu, Z. Su, J. Wang, S. Chen, and L.-L. Fu, 2018: Partitioning ocean motions into balanced motions and internal gravity waves: A modeling study in anticipation of future space missions. *J. Geophys. Res. Oceans*, **123**, 8084–8105, <https://doi.org/10.1029/2018JC014438>.
- van Meurs, P., 1998: Interactions between near-inertial mixed layer currents and the mesoscale: The importance of spatial variabilities in the vorticity field. *J. Phys. Oceanogr.*, **28**, 1363–1388, [https://doi.org/10.1175/1520-0485\(1998\)028<1363:IBNIML>2.0.CO;2](https://doi.org/10.1175/1520-0485(1998)028<1363:IBNIML>2.0.CO;2).
- Weller, R. A., 1982: The relation of near-inertial motions observed in the mixed layer during the JASIN (1978) experiment to the local wind stress and to the quasi-geostrophic flow field. *J. Phys. Oceanogr.*, **12**, 1122–1136, [https://doi.org/10.1175/1520-0485\(1982\)012<1122:TRONIM>2.0.CO;2](https://doi.org/10.1175/1520-0485(1982)012<1122:TRONIM>2.0.CO;2).
- Wenegrat, J. O., and L. N. Thomas, 2017: Ekman transport in balanced currents with curvature. *J. Phys. Oceanogr.*, **47**, 1189–1203, <https://doi.org/10.1175/JPO-D-16-0239.1>.
- Whitt, D. B., and L. N. Thomas, 2015: Resonant generation and energetics of wind-forced near-inertial motions in a geostrophic flow. *J. Phys. Oceanogr.*, **45**, 181–208, <https://doi.org/10.1175/JPO-D-14-0168.1>.
- Xie, J.-H., and J. Vanneste, 2015: A generalised-Lagrangian-mean model of the interactions between near-inertial waves and mean flow. *J. Fluid Mech.*, **774**, 143–169, <https://doi.org/10.1017/jfm.2015.251>.
- Young, W. R., and M. B. Jelloul, 1997: Propagation of near-inertial oscillations through a geostrophic flow. *J. Mar. Res.*, **55**, 735–766, <https://doi.org/10.1357/0022240973224283>.
- Zhai, X., H. L. Johnson, D. P. Marshall, and C. Wunsch, 2012: On the wind power input to the ocean general circulation. *J. Phys. Oceanogr.*, **42**, 1357–1365, <https://doi.org/10.1175/JPO-D-12-09.1>.

Copyright of Journal of Physical Oceanography is the property of American Meteorological Society and its content may not be copied or emailed to multiple sites or posted to a listserv without the copyright holder's express written permission. However, users may print, download, or email articles for individual use.